UNIVERSITÀ POLITECNICA DELLE MARCHE
Repository ISTITUZIONALE

Order calibrated functional beamforming for constant mainlobe width

(Article begins on next page)

26 December 2024

Order Calibrated Functional Beamforming for constant mainlobe width

Gianmarco Battista[a], Paolo Chiariotti[b,*], Alfredo Cigada[b], Paolo Castellini[a]

[a]Università Politecnica delle Marche,
Department of Industrial Engineering and Mathematical Sciences, 60131 Ancona, Italy
[b]Politecnico di Milano,
Department of Mechanical Engineering, Via Giuseppe La Masa 1, 20156, Milano, Italy

Abstract

This paper introduces a beamformer with constant mainlobe width over a given frequency range based on the well-known Functional Beamforming. In fact, one of the main issues with Conventional and Functional Beamforming is the worsening of spatial resolution towards lower frequencies. The idea presented here is to exploit the order (exponent in its typical formulation) of Functional Beamforming as a leverage to maintain the same mainlobe width for different analysis frequencies. A strategy for accurately measure the mainlobe size is described and exploited for characterizing any array used in the beamforming analysis. An order calibration procedure, which boils down to the estimation of two fitting coefficients describing the proper beamformer order, is proposed. The procedure resulted useful to achieve a constant mainlobe size across a given frequency range. The validity of the whole approach is demonstrated on both synthesized and experimental data.

Keywords: `Beamforming, microphone array, acoustic measurements, aeroacoustics`

---

*Corresponding author
Email address:* `paolo.chiariotti@polimi.it` (Paolo Chiariotti)

1. Introduction

Acoustic source mapping based on phased microphone array measurements is a well-established technology for characterizing noise sources with applications in many engineering field. In fact, the advantages with respect to single microphone measurements is related to the possibility of localizing and quantifying different source contributions. Some of the typical applications are the characterization of aeroacoustic noise generated by airfoils [1], aircrafts [2] or the characterization of noise produced by rotating machinery [3, 4, 5]. A comprehensive review of the various algorithms and applications associated to phased array measurements is provided by Chiariotti et al [6], while a review targeted to aeroacoustic applications is provided by Merino-Martinez et al in [7]. Several classifications of acoustic imaging techniques are available in literature: they mainly differ for the approach adopted or the calculation domain. As frequency domain approaches are concerned, which are the target of this paper, a systematic theoretical classification was proposed by Leclère et al in [8]. Three main methodology classes can be distinguished: beamforming, deconvolution techniques and inverse methods. Most of these approaches require the identification of a spatial Region of Interest (RoI) to be used as target calculation region, the acoustic discretization of that region by the placement of potential elementary sources (plane waves, monopoles, dipoles, etc.) at known locations and the assumption of an acoustic propagation model. Different aspects can be considered in the model, in addition to the direct propagation path, like cavity modes, scattering, image source and others. The main difference among these approaches rely in the way that potential source coefficients are calculated from pressure measurements.

Beamforming methods estimate the potential source coefficients one by one. In fact, a beamformer is a spatial filter which lowers the contributions outside the beamformer focalization direction/point. Therefore, the acoustic map is obtained by focusing the array on a single potential source in turn, as if it

2

were the only active one. Beamforming methods are widely adopted, especially in commercial systems, since they are generally quick and easy to implement. However, the source levels on the map are normally inaccurate in case of multiple sources since the maps are spoiled by the array spatial response, commonly named Point Spread Function (PSF). This introduces blurring and artefacts in the acoustic map because the spatial filter is not ideal. For example, a point source is mapped by a beamformer with a lobe having finite size, i.e. the mainlobe, and this aspect limits the ability of beamformers in distinguishing neighboured sources. Moreover, several artefacts, named sidelobes or "ghost images", are introduced, which may produce misinterpretation of the maps and limit the actual dynamic range in the source identification. To overcome beamforming limitations, deconvolution techniques have been developed. The objective of a deconvolution process is to remove the PSF from the beamforming maps to retrieve the actual sound source distributions ([9, 10, 11]). Contrarily to beamforming approach, inverse methods aim at solving the full acoustic mapping problem, thus returning the source coefficients for the whole set of potential sources. Several inverse techniques were developed over the years, such as Nearfield Acoustic Holography [12], Generalised Inverse Beamforming [13], Covariance Matrix Fitting [14, 15, 1], Bayesian Approach to sound source reconstruction [16], Equivalent Source Method with tailored solvers [17, 18]). Both deconvolution of beamforming maps and inverse methods require to solve an inverse problem with a degree of freedom for each source coefficient. This is in contrast with beamforming approaches, as these latter methods estimate each source coefficient separately. Surely, deconvolution and inverse methods leads to maps with fine spatial resolution and high accuracy in source quantification, but the complexity of implementation may not be justified in some applications.

As in several application such an increased complexity is neither affordable nor tolerated, this paper focuses on the use of frequency domain beamforming, rather than deconvolution or inverse methods, with the aim of improving the accuracy of the identification process with no substantial increase of calculation

3

complexity with respect to a typical beamformer. The key of the proposed idea grounds on one of the main issues characterizing Conventional Beamforming (CB) [19], i.e. the dependency of the mainlobe width (MLW) from the frequency of analysis. In fact, the blurring effect due to the PSF of the array increases towards lower frequencies, thus worsening the spatial resolution. This characteristic of CB causes different lobe sizes in the acoustic map for different frequencies, despite the real sources keep the same spatial extension. This aspect is an issue when maps at different frequencies are analysed and compared or when maps are summed over a certain frequency range. In such a case, it is desirable to have a constant MLW for the whole range of interest. This goal can be achieved by exploiting the peculiarity of Functional Beamforming (FB), introduced by Dougherty [20] with the aim of enhancing the performance of traditional CB. In fact, the FB output is governed by the ν order, which allows the main lobe to be narrowed and the sidelobes to be lowered; as a result, beamformer performance can be improved in terms of both spatial resolution and dynamic range. However, in the standard usage of FB, the same order is set for the whole frequency range, thus having again the same dependency of the mainlobe size from the frequency.

The idea presented in this paper is to exploit the order ν of FB as a leverage to keep constant the MLW when beamforming maps are calculated over a certain frequency range. To the best of authors' knowledge, this strategy has not been explored in literature yet, nor exploited in any practical applications. This variant of FB is addressed in this paper as Order Calibrated Functional Beamforming (OC-FB). The first step of this work is to define a method for the measurement of MLW. This enables to characterise the MLW of FB versus order and frequency. The second step is to define a procedure to calculate the proper order enabling the design of a beamformer with constant mainlobe width, in a given frequency band. This paper therefore does not aim at presenting a completely new beamforming method. Rather, it aims at discussing how to optimise the use and performance of an existing and powerful algorithm as FB

4

is, since it is widely used in several application fields. The paper is structured as follows: Section 2 briefly summarizes the theory and the basic principles of frequency-domain beamforming, Section 3 shows the approach adopted for the characterisation of FB in terms of mainlobe width, Section 4 describes two calibration procedures of OC-FB order to get the constant MLW, Section 5 shows the applications on both simulated and experimental data and, finally, Section 6 draws conclusions on the proposed method.

2. Basic principles and theory

2.1. Frequency Domain Conventional Beamforming

The beamforming techniques adopted in this paper are based on phased microphone array measurements. As notations are concerned, the term M relates to the number of microphones used in the array, while the location of a generic m microphone is addressed as $\mathbf{y}_m$; the term N addresses the total number of potential source locations over the calculation area, while the term $\mathbf{x}_n$ addresses the generic potential n-th source location. The Cross-Spectral-Matrix (CSM) estimated from the pressure signals measured by the M microphones is obtained exploiting the Welch's method [21].

In the classical application, the focusing/calculation area is a plane close to the target. However, a surface representing the object of interest [22] or a volumetric map [23, 17, 24] may be useful when a more general approach is required. Once the RoI is defined, it must be discretized with a set of elementary sources. In this work, only monopoles are chosen since it is the commonest choice in source mapping. However, also different source models can be adopted. After that, the model of an acoustic propagator must be defined. The simplest choice consists of a source-microphone free-field propagation. This choice is not mandatory, as many other aspects can be included in the propagation model. In frequency domain, the propagation at a single frequency is modelled by complex coefficients, $g_{n,m}$, for each source-receiver pair. It is useful to collect the coefficients, from the n-th source to all microphones, in a M-by-1 vector $\mathbf{g}_n$. When

5

adopting a pressure-to-pressure propagator formulation [23, 1] for a monopole point source placed at $\mathbf{x}_n$ the acoustic transfer function is

$$g_{n,m}(\mathbf{x}_n, \mathbf{y}_m, \mathbf{y}_0) = \frac{r_{n,0}}{r_{n,m}} \, \mathrm{e}^{\mathrm{i}\frac{2\pi f}{c}(r_{n,m}-r_{n,0})} \, , \tag{1}$$

where f is the frequency of analysis, c is the speed of sound in the medium and i is the imaginary unit. The point $\mathbf{y}_0$ is a reference point that is usually set in the geometric centre of the array. The terms $r_{n,0} = \|\mathbf{x}_n - \mathbf{y}_0\|_2$ and $r_{n,m} = \|\mathbf{x}_n - \mathbf{y}_m\|_2$ are the propagation distances from point source respectively to reference point and to microphones. The possibility to focus an array on a potential source location requires the definition of a spatial filter. In the beamforming framework, this filter is commonly named "steering vector". The steering vector is function of the acoustic propagator. Sarradj [23] analyzed four different steering vector formulations. In case of a single source, two formulations (I and IV) provide the exact source location, but fail in returning the correct level, while the other two (II and III) provide the exact source level with an error on the position. In this paper, the steering vector formulation IV, which is reported in Eq. 2, is adopted.

$$\mathbf{h}_n = \frac{1}{\sqrt{N}} \frac{\mathbf{g}_n}{\sqrt{\mathbf{g}_n^{\mathrm{H}}\mathbf{g}_n}} \, . \tag{2}$$

110

The term $\mathbf{g}_n$ represents a vector of size M, whose elements are expressed as in Eq. 1. The output of CB is the estimate of the n-th source power that is calculated by using the CSM and the steering vectors:

$$b_n = \mathbf{h}_n^{\mathrm{H}}\mathbf{P}\mathbf{h}_n \, . \tag{3}$$

The entire map is obtained by calculating the beamforming output for all the N potential sources by updating the steering vectors according to the focusing target.

115   The beamformer is characterised by the PSF which mainly depends on the number of microphones and their spatial arrangement, frequency and array aperture. For a planar array, the latter is defined as the diameter D of the

6

smallest circle containing all microphone locations. When array performance are evaluated and compared for different array diameters and frequencies, it is convenient to use the Helmholtz number (indicated with the symbol He), defined as $He = 2\pi D/\lambda = fD/c$. This non-dimensional number represents the ratio between array aperture and wavelength, therefore, it is intended to ease the analysis relying on the geometric similarity of array-waves interaction. The same approach is adopted in this paper for the distances, that are normalised by the array aperture D, unless differently specified.

Placing an ideal unitary point source at $\mathbf{x}_n$, which causes the pressure $\mathbf{g}_n$ at microphone locations, it is possible to evaluate the PSF of a beamformer. It is common to assess the performance of a particular array by means of two parameters obtainable from the PSF:

- Mainlobe Width (**MLW**): it is the extension of the region around the PSF main peak that is above -3 dB.

- Maximum Sidelobe Level (**MSL**): it is the level of the maximum local peak, excluding the mainlobe.
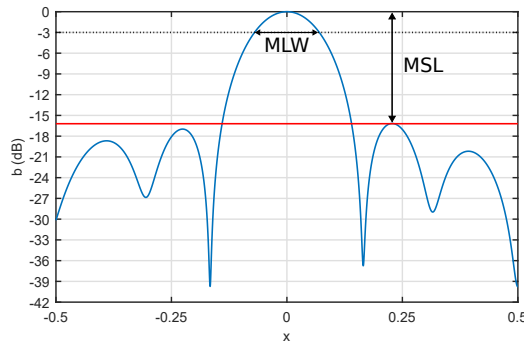

Figure 1: Example of 1D PSF obtained with CB (blue curve) and its main characteristics (MLW and MSL).

For clarity, Fig. 1 shows an example of MLW and MSL on 1-dimensional PSF. For a typical application it is useful to visualize the PSF on a plane parallel

7

to the array, as depicted in Figure 2. In this example, a $M = 40$ microphones Vogel spiral design with $V = 5$ is used [25].
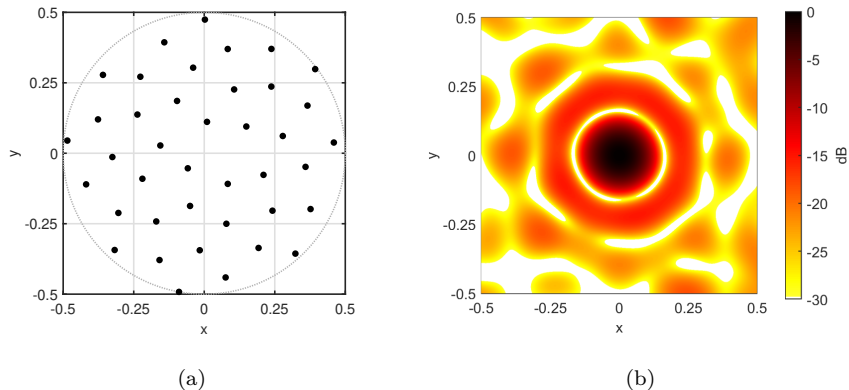

(a) (b)

Figure 2: Microphone array and PSF. Lengths are non-dimensionalised by the array aperture. (a) Vogel spiral ($V = 5$, $M = 40$) array layout. The dotted grey line is the array aperture. (b) Example of 2D PSF with CB.

2.2. Functional Beamforming

Functional Beamforming is a generalisation of CB which makes use of mathematical functions applied to the CSM to enhance the spatial resolution and increase the dynamic range of the beamformer. The output of FB is calculated as:

$$b_n(\nu) = \left[\mathbf{h}_n^{\mathrm{H}} \mathbf{P}^{\frac{1}{\nu}} \mathbf{h}_n\right]^{\nu} , \qquad (4)$$

140 where the parameter ν is the order of the beamformer. For $\nu = 1$ the beamformer reduces to be the same of CB. Figure 3 shows the effect of the order ν on the beamformer response. These maps highlight the improvements with respect to CB PSF depicted in Figure 2.
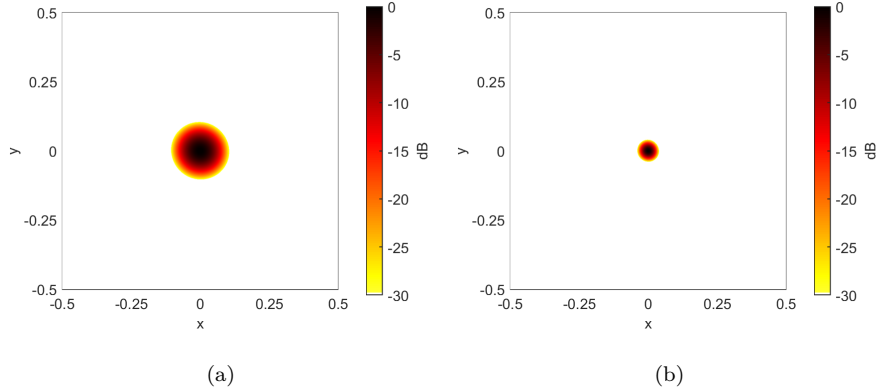
8

Figure 3: Example of 2D PSF with FB using a Vogel spiral ($V = 5$, $M = 40$) array layout.(a) FB order $\nu = 4$. (b) FB order $\nu = 40$.

145   The basis assumption of FB is that the PSF is exactly equal to 1 at the source location, hence $\mathbf{h}_n^{\mathrm{H}}\mathbf{g}_n = 1$. This means that by increasing the order ν the sidelobes decrease while the peak of the PSF remains unaltered. If this hypothesis holds, the FB response $b_n(\nu)$ is exactly the same of CB at the source location. However, in practical applications there is no perfect match between
150 the measured complex pressure and the steering vectors, hence the PSF peak is lower than 1, causing an underestimation of the level when ν is increased. A detailed analysis of this aspect is described in [26], where the propagation model errors are indicated as the main cause. In fact, Dougherty [20] highlights the importance to calibrate the array used in the measurements for an actual
155 exploitation of high values of ν. In [27], the reduction of level in FB maps due to a not perfect steering vector matching is corrected assuming that CB provides accurate levels. In fact, FB maps are scaled to match the peak level with the peak level of CB map, hence compensating the artefact level reduction due to model errors. Moreover, FB is not compatible with the diagonal removal
160 process, i.e. set the CSM diagonal entries to zero, that is typically exploited in CB (especially in aeroacoustic apllications) to remove microphones self-noise. Consequently, this process is not adopted in this paper. This limitation can be overcome adopting array denoising techniques like the diagonal denoising tech-

9

nique proposed by Hald [28], a probabilistic approach proposed by Dinsenmeyer et al [29] or the spherical harmonics decomposition method [30] in case spherical arrays are used.

3. Functional Beamforming mainlobe width characterisation

3.1. Measuring the Mainlobe Width

The Rayleigh criterion is commonly used for the assessment of the CB resolution limit [31]. However, this criterion derives from the assumption of continuous circular aperture and plane wave propagation. In real applications, these hypotheses are commonly not met since a finite number of sampling points are available (i.e. M microphones) and monopole sources (i.e. spherical waves) are often considered. This means that the actual spatial resolution, which is strictly related to the MLW, is not accurately known for the particular array in use. Therefore, a crucial aspect to face for the approach presented in this paper is the definition of a systematic method to measure the MLW. In this section, an approach for measuring the beamforming mainlobe width is described. All lengths are non-dimensionalized by the array aperture.

Consider a unitary monopole source placed on the array longitudinal axis at one diameter distance ($\mathbf{x}_s = [0, 0, 1]$) and the plane parallel to the array at the same distance of the source, as depicted in Figure 4(a). The beamformer output can be considered as a function of a generic point on the plane with respect to the source location, hence $b(\mathbf{x} - \mathbf{x}_s)$. It is convenient to rewrite the latter expression in polar coordinate system $b(r, \theta)$, with the origin in the source location $\mathbf{x}_s$, where $r = \|\mathbf{x} - \mathbf{x}_s\|_2$ (Figure 4(b)).
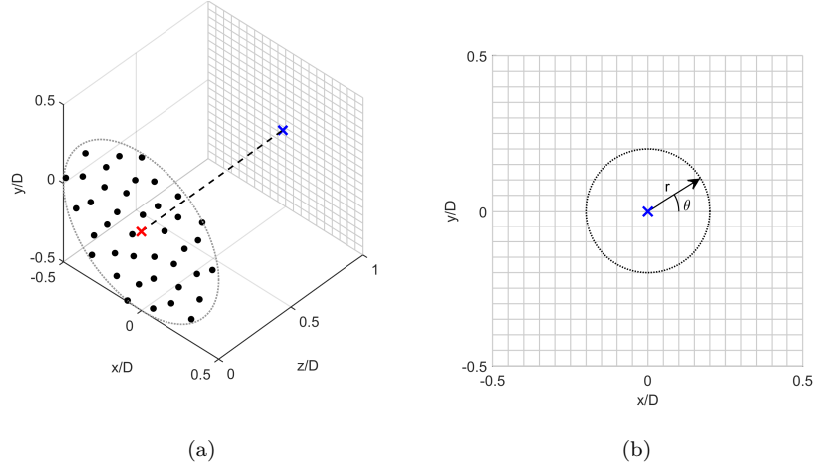
10

Figure 4: Array-source simulation setup for MLW measurement. The source is placed on the longitudinal array axis at one diameter distance from the array. All the axis scales are normalised by the array aperture. (a) View of relative position between microphone array (black dots) and monopole source $\mathbf{x}_s$ (blue cross). The red cross is the array centre and the grey dotted circle around the microphones is the array aperture. (b) View of the polar reference system, centred on source location $\mathbf{x}_s$ (blue cross), used for MLW measurement.

The beamformer output on a circumference of generic radius r can be averaged over the circumferential direction θ, for a number of K_θ discrete directions θ_k, thus leading to

$$b(r)_{\langle\theta\rangle} = \frac{1}{K_\theta} \sum_{k=1}^{K_\theta} b(r, \theta_k) \, . \tag{5}$$

This function is the average PSF on a circumference of generic radius r around the source location. The subscript $\langle\theta\rangle$ is used to indicate the mean of a function over K_θ values of a generic variable θ. The function $b(r)_{\langle\theta\rangle}$ is depicted in Figure 5, referring to the setup plotted in Figure 4(a).
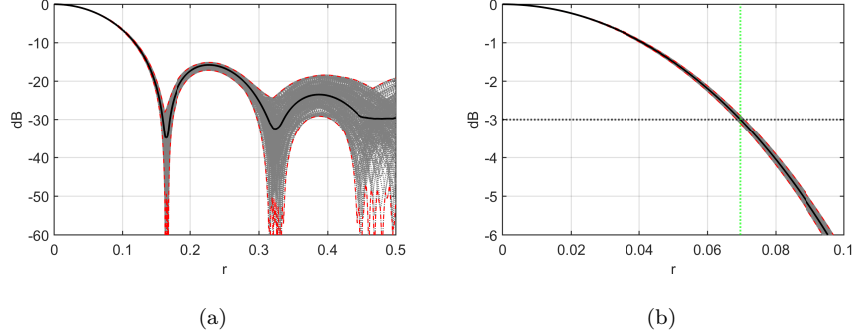
11

Figure 5: Plot of PSF in radial direction from source location. (a) Average radial PSF (black solid line) $b(r)_{\langle\theta\rangle}$. Grey dotted curves represents $K_\theta = 360$ equally spaced radial PSF ($b(r, \theta_k)$). Red dashed curves represents the maximum and minimum radial PSF among those shown. (b) Zoom on the mainlobe. Vertical green line is the mainlobe radius, i.e. one half of the MLW.

From the definition of MLW given in the previous section, it follows that the quantity defined in Eq. (5) can be used to measure the MLW by finding the zero of the following function:

$$B(r) = \left| 10 \log_{10} \left(\frac{b(r)_{\langle\theta\rangle}}{b(\mathbf{x}_s)} \right) + 3_{\mathrm{dB}} \right| . \tag{6}$$

Therefore, at the mainlobe radius R_{ML}, i.e. the half of the MLW, it occurs:

$$B(R_{\mathrm{ML}}) = 0 . \tag{7}$$

When and where the condition expressed in Eq. (7) is met, the average value of the mainlobe on the circumference turns out to be –3 dB. This method provides the exact MLW in case of perfectly axial-symmetric mainlobe; it returns an approximation of the mainlobe with a circumference otherwise. Figure 6 shows some examples of MLW measurements with the proposed approach. Three examples are shown:

- Example 1: on-axis source at $He = 4$,

- Example 2: on-axis source at $He = 8$,

- Example 3: off-axis source at $He = 8$.

12

In all the examples presented here, the source is placed on the plane at one diameter distance from the array plane. The mainlobe of on-axis sources has an almost symmetric shape, while for off-axis source location, the mainlobe has an

205 ellipsoidal shape that brings to a greater MLW with respect to on axis source in the same condition (i.e. same frequency and source-array plane distance). In Figure 7, also the beamformer output with respect to circumferential direction on the mainlobe radius $b(R_{\mathrm{ML}}, \theta)$ is depicted. These curves shows that there are smaller fluctuations of CB output for in-axis source, while off-axis source

210 lobe has stronger fluctuations, due to non axial-symmetric shape. However, the MLW measurement mechanism described here is capable to assess a sort of "equivalent mainlobe size" also in presence of a "distorted" lobe shape. Therefore, this approach can be adopted to precisely measure the MLW for any planar microphone array layout and it is compatible also with FB.
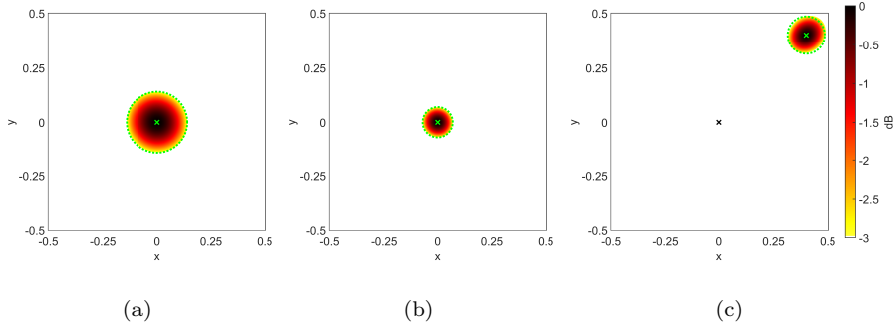

(a) (b) (c)

Figure 6: Visualization of CB mainlobe and measured MLW. Green dotted lines is the main-lobe circumference and green cross is the source location. (a) Example 1: on-axis source at $He = 4$ ($R_{\mathrm{ML}} = 0.140$). (b) Example 2: on-axis source at $He = 8$ ($R_{\mathrm{ML}} = 0.070$). (c) Example 3: off-axis source at $He = 8$ ($R_{\mathrm{ML}} = 0.085$), black cross is the array axis.
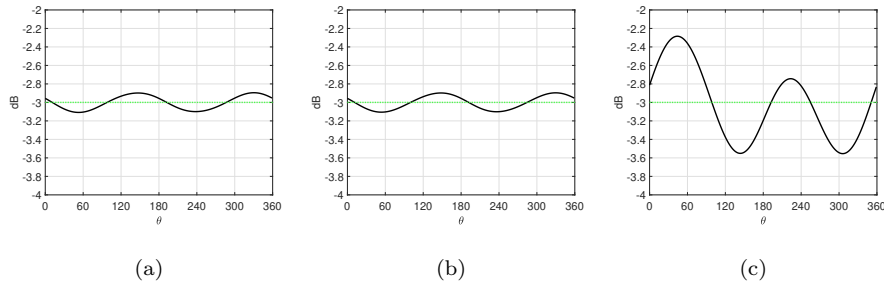
13

Figure 7: Beamformer output profile on circumference having the measured mainlobe radius R_{ML}. (a) Example 1: on-axis source at $He = 4$. (b) Example 2: on-axis source at $He = 8$. (c) Example 3: off-axis source at $He = 8$.

3.2. General characterisation of mainlobe versus frequency and order

The approach described in the previous section makes it possible to systematically characterise the MLW of FB, as function of Helmholtz number and beamformer order. An example of this kind of analysis is provided here for a Vogel spiral array layout with $V = 5$ and $M = 40$ (Figure 2) by considering again the setup shown in Figure 4. The trend of R_{ML} is evaluated in the frequency range $He = [4; 32]$, and in the order range $\nu = [1; 500]$. The outcome is that the mainlobe size has an almost linear behaviour with respect to frequency and order in logarithmic scale. This suggests a simple analytical expression to approximate the mainlobe radius dependency from Helmholtz number and beamformer order:

$$R_{\mathrm{ML}}(He, \nu) = a_0 \cdot H^{a_1} \cdot \nu^{a_2} \, . \tag{8}$$

Applying the natural logarithm to both members, Eq. 8 becomes:

$$\log(R_{\mathrm{ML}}(He, \nu)) = \log(a_0) + a_1 \log(H) + a_2 \log(\nu) \, . \tag{9}$$

In this form, a Least-Squares linear fitting approach can be used to estimate the coefficients a_1 and a_2, and the constant term $\log(a_0)$ for the example data. The values obtained, with a coefficient of determination $R^2 = 0.999$, are $\log(a_0) = -0.658$, $a_1 = -0.995$ and $a_2 = -0.440$. As expected, the mainlobe radius is approximately proportional to the reciprocal of the frequency,

14

indicated by a_1, while the most interesting result is the trend of R_{ML} with respect to the FB order ν, indicated by a_2. Clearly, this outcome is not valid for any array, but it helps addressing the definition of a general approach for obtaining a constant MLW by properly setting the beamformer order.

Aiming at the generalisation of this approach, it turns useful to define the normalised Helmholtz number (indicated with the symbol Hn) by choosing a reference frequency, and calculating the correspondent Helmholtz number (indicated with the symbol He_{ref}), thus leading to $Hn = He/He_{\mathrm{ref}}$. The reference frequency is used to define the corresponding reference mainlobe radius $R_{\mathrm{ML,ref}}$ for $\nu = 1$, i.e. the MLW of CB, that is employed for normalization of the mainlobe radii. In such way, Eqs. (8) and (9) become:

$$Rn(Hn,\nu) = Hn^{a_1} \cdot \nu^{a_2} \,, \tag{10}$$

$$\log(Rn(Hn,\nu)) = a_1 \log(Hn) + a_2 \log(\nu) \,, \tag{11}$$

where the left sided term is the normalised radius $Rn = R_{\mathrm{ML}}/R_{\mathrm{ML,ref}}$. One of the advantages in adopting normalised frequency Hn and radius Rn is that the term a_0 can be fixed at 1, since for $Hn = 1$, and $\nu = 1$, the normalised radius is $Rn = 1$ by definition. As consequence, Eqs. (9) and 11 differ only by an offset. This aspect will be important in the determination of a general law for ν. The trend coefficients estimated in the form of Eq. (11) ($He_{\mathrm{ref}} = 32$) become $a_1 = -0.973$ and $a_2 = -0.447$, with a coefficient of determination $R^2 = 0.998$.

The same analysis has been repeated in a systematic way for a variety of array designs to understand how these affect the trend of mainlobe radius versus frequency and order. A set of different array layouts is generated by changing the parameter V of Vogel spirals, while the number of microphones is kept constant ($M = 40$). A list of 46 values of V, between 0.1 and 5, with a step of 0.1, is selected. The values $V = 1$ and $V = 4$ are discarded since they provide

15

240 linear arrangements. Also values close to them are discarded to avoid quasi-linear microphone arrangement for some values of M. An aspect to mention is that the microphone distributions generated in this test have the same radial distribution (to ensure this condition, the parameter H - see [25], was set as $H = 0$), which corresponds to absence of radial weighting. Anyway, all the concepts

245 explained in the present paper hold for every radial microphone distribution. The distribution of fitting coefficients a_1 and a_2 for different array design is shown in Figure 8. As expected, the exact values are design-dependant, but they are all still close to the average values. For all the arrays considered, the fitting determination coefficient is $R^2 \geq 0.997$.
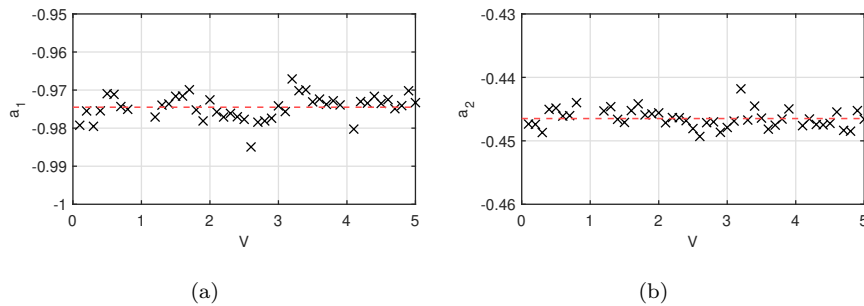

(a)   (b)

Figure 8: Trend coefficients of MLW for different array design ($M = 40$) where the V parameter of the Vogel spiral is changed;. Frequency range: $He = 4$–32, i.e. $Hn = 0.125$–1. Order range $\nu = 1$–500. (a) a_1. (b) a_2.

250 A further step of analysis is performed, in order to verify the impact of the number of microphones in the procedure. Using the same list of V adopted in the previous test, a larger variety of arrays is simulated by changing the number of microphones in each array - M ranging from 20 to 160 with a step of 10. This resulted in a dataset of 644 different array layouts. Figure 9 shows the trend

255 of both coefficients a_1 and a_2 with respect to the number of microphones. The average values of the two coefficient distributions seem to tend approximately to $a_1 \approx -0.98$ and $a_2 \approx -0.45$ as M increases. The standard deviation values associated to the same coefficients distributions decrease as M increases. More-over, also the Pearson correlation coefficient tends to $R^2 > 0.998$. Certainly,

16

these indications are valid for a number of microphones ranging from 20 to 160, but the majority of arrays exploited in practical applications fall in this range. Observing Figure 9(d), it is well evident that the linear model adopted in the fitting produces non-random residuals on the average. This means that there is a more complex behaviour of R_{ML} that is not fully represented by the linear model. Further considerations about the model will be discussed in Section 4. The outcome of this analysis indicates that the changes of the MLW with respect to order and frequency are weakly dependant from the array design. This is important for a definition of a general model and a procedure to control the mainlobe size by properly acting on the beamformer order ν.
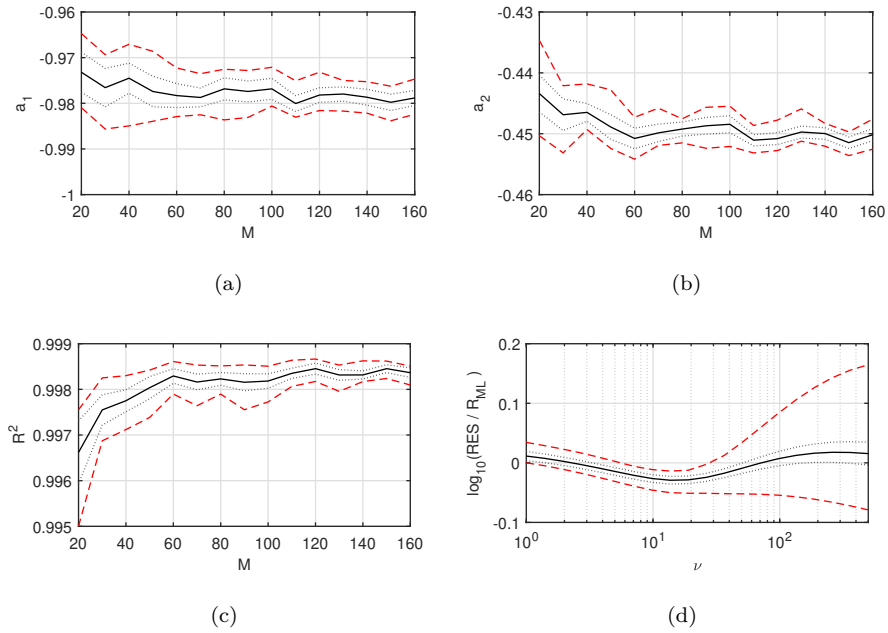

Figure 9: Statistics of fitting parameters. Microphone number range: $M = 20$–160. Vogel spiral parameter range: $V = 0.1$–5. Frequency range: $He = 4$–32, i.e. $Hn = 0.125$–1. Order range $\nu = 1$–500. Black solid line: average values. Grey solid line: average $\pm$ one standard deviation. Red dashed line: maximum and minimum values. (a) a_1. (b) a_2. (c) R^2 (d) Fitting residuals. Relative values are calculated with respect to R_{ML} provided by the linear model.

17

4. Functional Beamforming order calibration for constant mainlobe width

A sound and robust application of OC-FB requires the identification of a specific mathematical law for properly setting the beamformer order ν^* to obtain the target MLW. For practical implementation, it is convenient to identify

275 an explicit expression that returns ν^* as function of Hn. The function can be used for values $Hn \leq 1$, i.e. $He < He_{\mathrm{ref}}$, and returns beamformer orders $\nu^* \geq 1$. In the following, an Order Calibration Procedure (OCP) tailored to estimate this function, more specifically the fitting coefficients $(C_1, C_2, \ldots)$, for a given array is presented. The procedure is demonstrated on the Vogel array

280 layout depicted in Fig. 2 ($V = 5$, $M = 40$) and for the setup shown in Fig. 4, therefore, the calibration source is a in-axis monopole at one diameter from the array plane.

4.1. Order Calibration Procedure

This OCP procedure aims at a direct estimation of the proper order ν^* to maintain the mainlobe radius equals to $R_{\mathrm{ML,ref}}$. The beamformer order can be increased to nullify the difference between the reference radius $R_{\mathrm{ML,ref}}$ and the actual beamformer mainlobe radius $R_{\mathrm{ML}}(\nu, Hn)$ at a generic frequency $Hn \leq 1$. This can be formally expressed by the following condition

$$\Delta R_{\mathrm{ML}}(\nu^*, Hn) = 0 \,, \tag{12}$$

where the function $\Delta R_{\mathrm{ML}}(\nu, Hn)$ is defined as

$$\Delta R_{\mathrm{ML}}(\nu, Hn) = \left\| R_{\mathrm{ML}}(\nu, Hn) - R_{\mathrm{ML,ref}} \right\|_2 \,. \tag{13}$$

285 The value of ν^* from Eq. (12) can be obtained by means of a minimization process, since the function is non-negative and has a unique minimum. The approach described above can be adopted to characterise any array in detail, by calculating ν^* on a dense grid of He_{ref} and Hn, and use the result in form of

18

lookup table to select the proper beamformer order for the particular calculation.

However, a more efficient method is presented here. The steps of OCP can be summarized as:

1. define He_{ref}, hence the value of $R_{\text{ML,ref}}$;

2. find the values of ν^* with Eq. (12) for a set of $Hn \leq 1$;

3. fit data (Hn, ν^*) with a curve;

4. retrieve the calibration coefficients $(C_1, C_2 \dots)$, depending on the chosen fitting curve.

This procedure can be repeated for different reference frequencies He_{ref} to calculate an average value of calibration coefficients. The data (Hn, ν^*), are calculated for 20 exponentially spaced values $Hn = [0.125; 1]$ and for $He_{\text{ref}} = [8; 48]$. The outcome is depicted in Figure 10. The values of ν^* show very similar trend and begin to significantly differ only for $Hn < 0.3$.
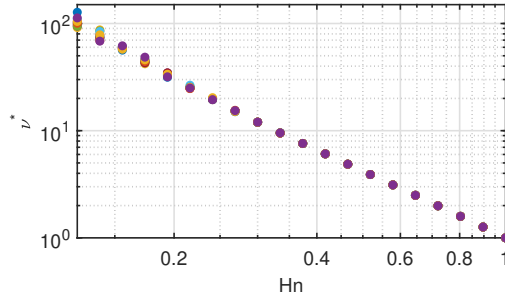

Figure 10: Orders for a constant MLW as function of normalised Helmholtz number ($Hn = [0.125; 1]$) for different reference Helmholtz number ($He_{\text{ref}} = [8; 48]$).

The choice of the fitting curve depends on the desired accuracy and the frequency range of application in terms of Hn. The authors suggest to fit the data in logarithmic scale with a polynomial curve of the type:

$$\log(\nu^*) = C_1 \log(Hn) + C_3 \log^3(Hn) \,. \tag{14}$$

This boils down to a polynomial fitting of the data with a cubic function. However, the constant and the quadratic terms are constrained to zero. The constant

19

term is set to zero to force the value $\nu = 1$ for $Hn = 1$, while only the cubic term
is adopted to model the non-linearity of the curve, since it is the most efficient.
This is a trade-off between accuracy in predicting the order, extension of the
frequency range and simplicity of the fitting function. For a linear fitting the
constant C_3 can be forced to zero. Both cubic and linear fitting in the Least-
Squares sense are applied to the whole set of data obtained for $He_{\mathrm{ref}} = [8; 48]$,
thus leading to the fitting curves shown in Fig. 11.

(a)

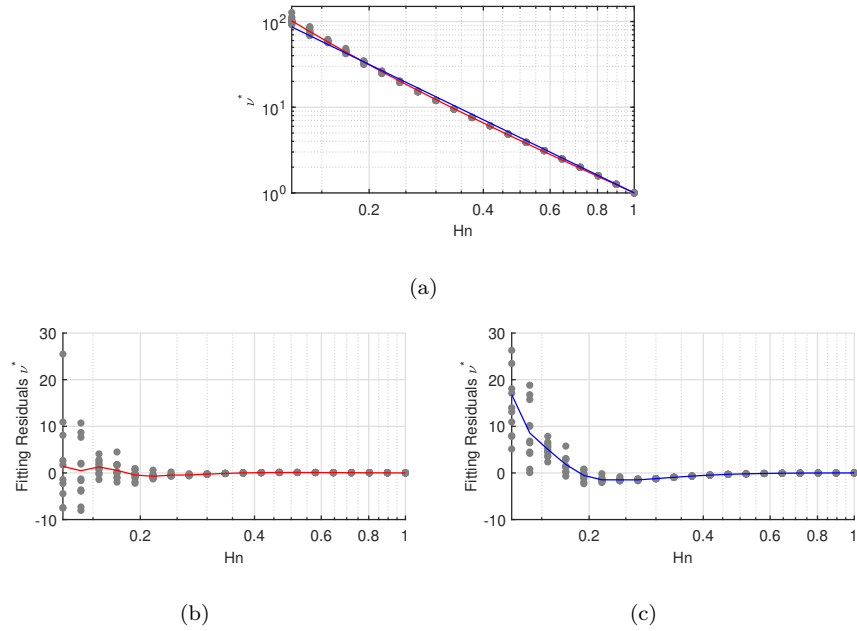(b)   (c)

Figure 11: Characterisation of array with OCP by fitting (ν^*, Hn) data. (a) Red curve is the
cubic fitting as in Eq. (14). Blue curve is the linear fitting. (b) Residuals of cubic fitting.
Red curve is the average of residuals. (c) Residuals of linear fitting. Blue curve is the average
of residuals.

The values of calibration coefficients for data related to a single He_{ref} are
shown in Figures 12 and 13. The lines (red in the color-version of the paper)
represent the average value of $C_{1\langle He_{\mathrm{ref}}\rangle}$ and $C_{3\langle He_{\mathrm{ref}}\rangle}$, obtained from the fitting
of data merged together among all the values of He_{ref}. In this case, the linear
fitting returns $C_{1\langle He_{\mathrm{ref}}\rangle} = -2.1448$, while the cubic one $C_{1\langle He_{\mathrm{ref}}\rangle} = -2.0102$
and $C_{3\langle He_{\mathrm{ref}}\rangle} = -0.0493$.

20
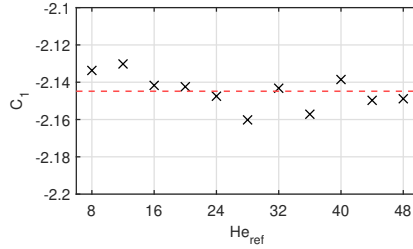
(a)

Figure 12: Characterisation of array with OCP - Linear fitting coefficients vs He_{ref}
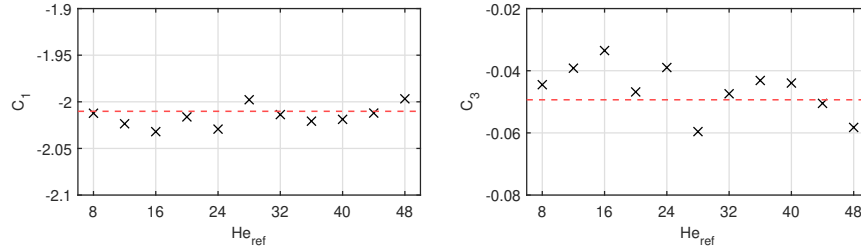
(a)   (b)

Figure 13: Characterisation of array with OCP - Cubic fitting coefficients vs He_{ref}

4.2. Variability of calibration coefficients

All the concepts discussed above in the paper are supported by the results obtained with the calibration source $\mathbf{x}_s$ on the longitudinal array axis at one

320 diameter distance. However, it is important to test the validity of the approach when the calibration source spans a wider region. With this purpose, the calibration coefficients are calculated with the source on planes located at different distances from the array plane and at different angles with respect to the array longitudinal axis. The region covered by the calibration source is a triangular

325 area on the plane $y = 0$. The angle ranges from -45 deg to 45 deg with 5 deg step, while, the distance of the source plane ranges from 0.5 to 8 diameters from the array (in particular: 0.5, 1, 2, 4 and 8). For each source position the same list of He_{ref} and Hn of the previous sections is used, thus resulting in 1140 calibration cases (95 source position times 12 reference frequencies). The
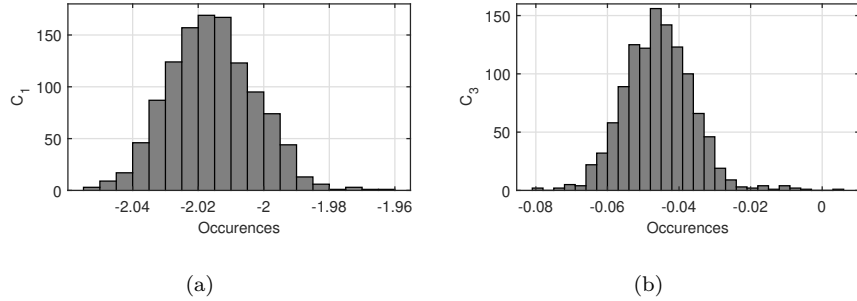
21

Figure 14: Histogram of calibration coefficients with the monopole source spanning on a conical region obtained using OCP. The cone covers a region from -45 deg to 45 deg and a distance from 0.5 to 8 diameters.

calibration coefficients are obtained with OCP and cubic fitting and have the distribution depicted in Figure 14. The value of the averaged coefficients are $C_{1\langle He_{\text{ref}}, \mathbf{x}_s \rangle} = -2.0100$ and $C_{3\langle He_{\text{ref}}, \mathbf{x}_s \rangle} = -0.0497$, that are close to those values obtained with on-axis source only. Moreover, all the coefficients are well aggregated near the average value, meaning that the calibration with on-axis source is representative enough of the relation between ν^* and Hn for the array under study. This aspect is crucial for the practical implementation of OC-FB. In fact, this allows OCP to be performed even once for a given array since the calibration coefficients remain valid for very different application scenarios, independently from source location and the reference frequency.

4.3. Guidelines in the choice of reference value (frequency or radius)

Once the OCP is performed on the array in use, the application of OC-FB requires to set a reference frequency, in terms of He_{ref}. However, the same choice can also be made in terms of $R_{\text{ML,ref}}$, since it exists a unique relationship between the mainlobe radius of CB and the frequency, once the source position is fixed. Therefore, the reference can be equivalently defined as a frequency He_{ref} or as a mainlobe target radius $R_{\text{ML,ref}}$. The choice is arbitrary and depends on what is more convenient for the user or on the target application. Despite no theoretical restrictions exist, some guidelines about this choice are

22

discussed in this section.

The most straightforward strategy is to set the mainlobe target radius $R_{\mathrm{ML,ref}}$ by considering the grid spacing of the map and the desired spatial resolution. However, the drawback of this approach is that the order ν^* may reach too high values, for broad frequency ranges, thus returning unreliable maps. In fact, an important aspect to consider is the maximum beamformer order ν^* that can be exploited considering the quality of microphone array calibration (compensation of errors in relative microphone positions and amplitude/phase mismatch between sensors). Dougherty [20] states that a well calibrated array supports FB order up to 200, or even higher, while an uncalibrated array is limited to maximum orders around 30. Therefore, considering that ν^* increases towards low frequencies, the He_{ref} value can be retrieved by imposing that the maximum order supported by the array is reached at the minimum frequency of analysis. Another possible strategy, which avoids the problem of exceeding the maximum order supported by the array, is to divide the entire analysis frequency range into several bands (e.g. one-third octave bands) and set the reference frequency equal to, or higher than, the upper limit of each band. In such way, the actual mainlobe radius trend is a stepped curve that increases towards low frequency. This strategy brings the benefit of having the spatial resolution constant within each band, while maintaining a limited value of the order in the whole frequency range of interest.

5. Results

5.1. Simulated data

In this section, the results of simulated experiments are presented. The aim of this section is to highlight differences between the acoustic maps obtained with CB and OC-FB on ideal noise-free data generated with the theoretical acoustic propagator of Eq. (1). The array adopted here is the same discussed in Section 4 , i.e. the Vogel array layout depicted in Fig. 2 ($V = 5$, $M = 40$).

The order ν^* to achieve a constant MLW with OC-FB is set following OCP, i.e. according to the procedure described in Section 4.1. In particular, the curve obtained from the cubic fitting (Eq.(14)) is chosen with the average coefficients $C_{1\langle He_{\mathrm{ref}}\rangle}$ and $C_{3\langle He_{\mathrm{ref}}\rangle}$. Three different simulated experiments are conducted:

- Simulation 1 (S1): one monopole source on array axis at $\mathbf{x}_s = [0, 0, 1]$;

- Simulation 2 (S2): two closely spaced monopole sources at $\mathbf{x}_s = [\pm 1/20, 0, 1]$;

- Simulation 3 (S3): linear source (the segment connects the source locations of S2).

It is well evident that, in all the simulations, the sources lay on the plane at one diameter of distance from the array, analogously to the setup shown in Figure 4(a). The reference frequency is set at $He_{\mathrm{ref}} = 32$, considering the speed of sound as 343 m/s.

An overview of MLW across the frequency range is provided in Figure 15. In fact, Figure 15 shows the trend MLW as function of frequency. This is provided through the use of the Helmholtz number, in 1-dimensional acoustic maps (corresponding to the line $y = 0$). These maps are depicted with 3 dB of dynamic range and normalised by the maximum for each frequency in order to highlight the extension of the mainlobe. From the map of OC-FB, it is well evident that the MLW remains fixed for frequencies below the reference Helmholtz number, while CB shows mainlobe size variations across the frequency range. It is worth noticing for OC-FB that some small fluctuations of the mainlobe size are present for $He < 8$. This is due to the fact that the fitting curve for ν^* does not perfectly match the fluctuations of the exact value calculated in the OCP approximately for $Hn < 0.25$ (see Figure 11). For $He \geq He_{\mathrm{ref}}$, CB and OC-FB are equivalent since $\nu = 1$ is set such frequency range.
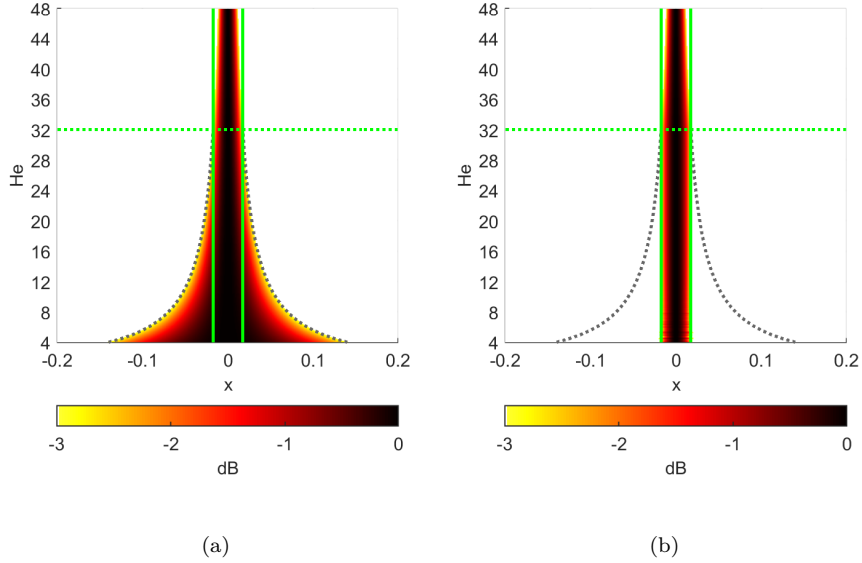
24

Figure 15: Simulation 1. 1D acoustic maps versus frequency for $y = 0$. The map at each frequency is normalised by its maximum and plotted with 3 dB of dynamic range. The horizontal dotted green line (colour-version only) addresses the reference frequency $He_{\mathrm{ref}} = 32$, while the two vertical green solid lines (colour-version only) represent the reference MLW. The grey dotted curves indicate the MLW for CB. (a) CB. (b) OC-FB.

The second experiment aims at demonstrating the benefit of OC-FB in terms of closely-spaced sources separation for frequencies below He_{ref} (Figure 16). The benefits of FB in terms of spatial resolution and dynamic range with respect to CB are well-known. The OC-FB combines these benefits with the constant spatial resolution for a wide frequency range.
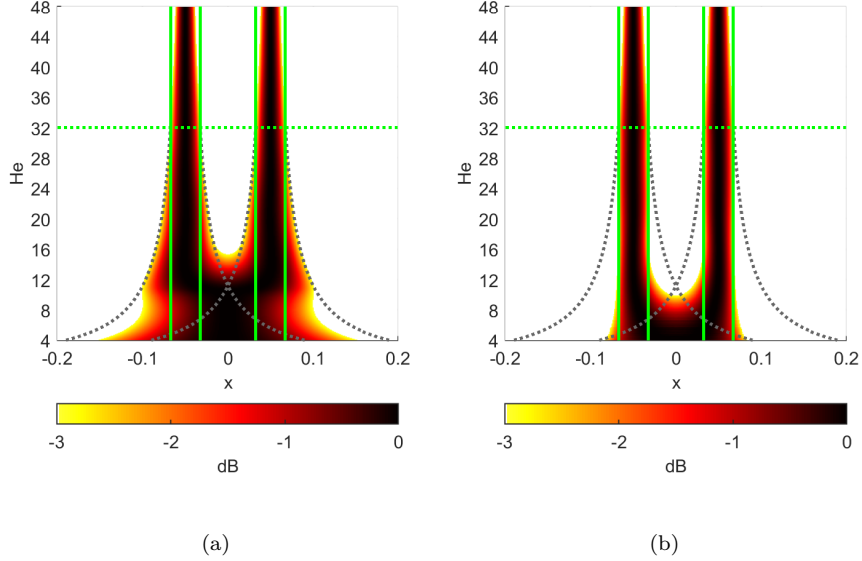
25

Figure 16: Simulation 2. 1D acoustic maps versus frequency for $y = 0$. The map at each frequency is normalised by its maximum and plotted with 3 dB of dynamic range. The horizontal dotted green line indicates the reference frequency $He_{\mathrm{ref}} = 32$, while the two vertical green solid lines represent the reference MLW. The grey dotted curves indicate the MLW for CB. (a) CB. (b) OC-FB.

The last simulated experiment (S3) involves a linear uncorrelated source, that is representative of the behaviour of beamformers in case of extended sources. This kind of source is well approximated by a series of aligned and closely spaced uncorrelated monopoles. Figure 17 shows again the differences between CB and OC-FB. Moving towards lower frequencies, both techniques fail to map the linear source correctly. However, OC-FB still shows an improvement for low frequency, especially below $He < 12$, since the extension of mapped source do not increase significantly as it does for CB. This represents a common limit of many beamformers when dealing with spatially extended sources.
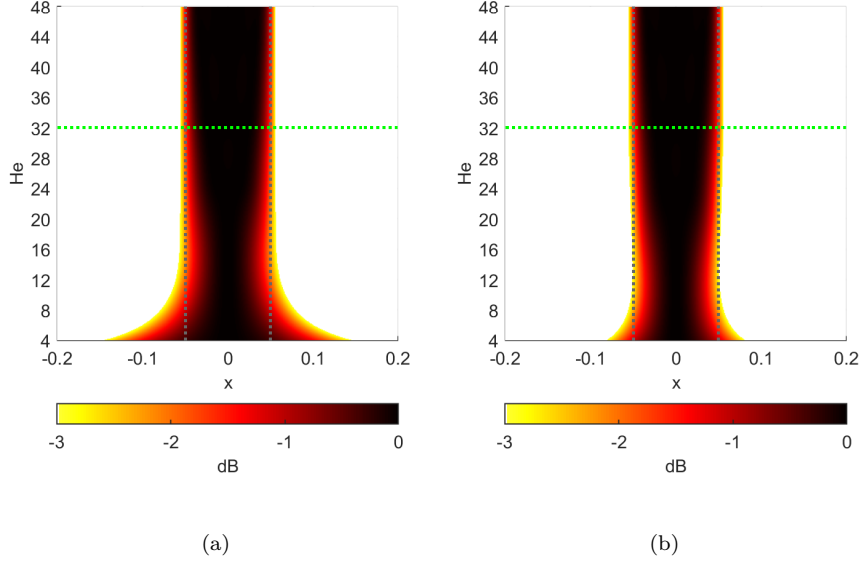
26

Figure 17: Simulation 3. 1D acoustic maps versus frequency for $y = 0$. The map at each frequency is normalised by its maximum and plotted with 3 dB of dynamic range. The horizontal dotted green line indicates the reference frequency $He_{\text{ref}} = 32$, while the two vertical dotted grey lines represent the exact source extension. (a) CB. (b) OC-FB.

5.2. Experimental aeroacoustic data

420   The goal of the application presented here is to discuss the behaviour of OC-FB with respect to CB in case of complex noise sources and in presence of relevant background noise. The experiment shown in this section is the same presented in [32] and it was performed in an aeroacoustic wind tunnel at Brandenburg University of Technology. The object under study is a NACA 0012 425 airfoil having a span of 0.28 m and a chord length of 0.25 m. The airfoil is placed in an open jet with a diameter of 0.2 m and core velocity of 50 m/s. These parameters are used to simulate the acoustic propagation in an open jet by means of *Acoular* open source software [33]. The outcome of this calculation are the actual travelling distances of the source-microphone path, therefore, 430 the distances calculated in such way are used in Eq. (1) instead of geometric distances. Boundary layer tripping was realized with a 2.5 mm anti-slip tape ap-

27

plied at 10% of the chord, both on suction and pressure side. The measurement
setup and the mapping plane are depicted in Figure 18. The region of interest
is discretised with a regular grid of monopoles with a step of 1 cm on the x and
y directions. The array, which embeds 56 microphones and has an overall di-
ameter of 1.3 m, is placed 0.715 m above the airfoil plane, outside the flow. The
total acquisition time is 40 s, at a sampling rate of 51.2 kHz. The time signals
are processed to estimate the CSM by averaging the cross-spectra over 2000
blocks of 2048 samples with 50% of overlap, thus having 25 Hz of frequency res-
olution. The Hanning window is applied on time signals before FFT calculation.

The calibration of the beamformer order is made with OCP by placing a
monopole on the array axis perpendicular to the array plane, at same distance
of the airfoil. The resulting average calibration coefficients for a cubic fit are
$C_{1\langle He_{\text{ref}}\rangle} = -1.9789$ and $C_{3\langle He_{\text{ref}}\rangle} = -0.0455$, for He_{ref} ranging from 8 to 48
and Hn from 0.125 to 1. For this case, the OC-FB is applied with $He_{\text{ref}} = 40$
corresponding to about 10675 Hz (with speed of sound 346.95 m/s).
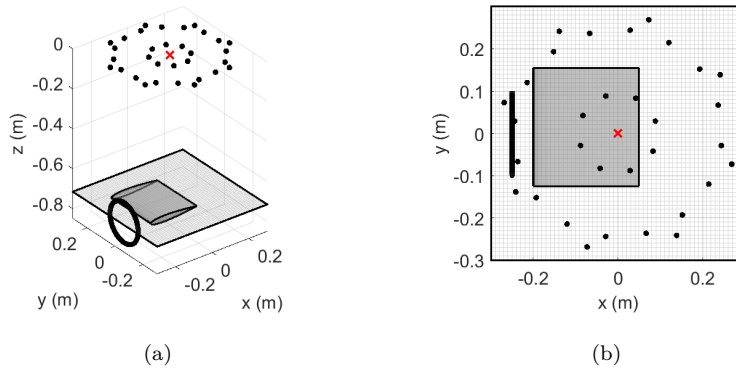

(a)

(b)

Figure 18: Experimental measurement setup and mapping plane. The black dots represents
the 56 microphones, while the red cross is the array centre. Black circle is the nozzle of the
open jet. (a) 3D view. (b) Top view.

The acoustic maps calculated with CB and OC-FB, for one-third octave

bands from 2 kHz to 8 kHz, are shown respectively from Figure 19 to 25, with a dynamic range of 10 dB. In all the maps, OC-FB reduces the blurring of sources with respect to CB, thus making the maps more consistent between the bands and allowing a better identification of the target noise sources. The other noticeable and expected effect is the increase of the dynamic range due to the usage of FB order greater than one. In fact, the sidelobe suppression is higher towards low frequency due to the increasing ν^* order. On the contrary, the source size increases for the lowest bands. This fact can have two causes. On the one hand, the actual source size increases for these frequencies; on the other hand, the effectiveness in maintaining the spatial extent of the sources gradually diminishes in the lower bands. In fact, the calibrated order ν^* exceeds 30 below $He = 8$.

Another noteworthy aspect concerns the 8 kHz map. In this case, the benefit of OC-FB on the dynamic range is limited. In fact, this band is quite close to He_{ref}, therefore, the calibrated order ν^* ranges from 1.41 to 2.23 only. This means that the increment of dynamic range would be small even in ideal conditions. Moreover, other tests (not shown in the paper) revealed that the dynamic range does not increase even with higher orders due to the presence of low signal to noise ratio in this frequency band.
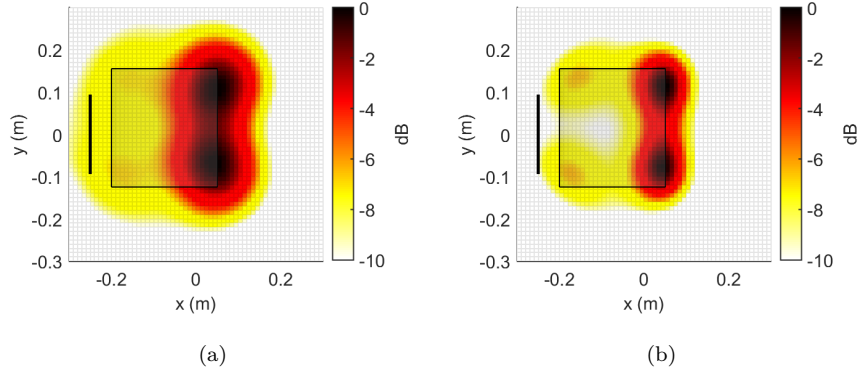
Figure 19: Acoustic maps of airfoil for 2 kHz one-third octave band, corresponding to $He = [6.7; 8.3]$. (a) CB (b) OC-FB.
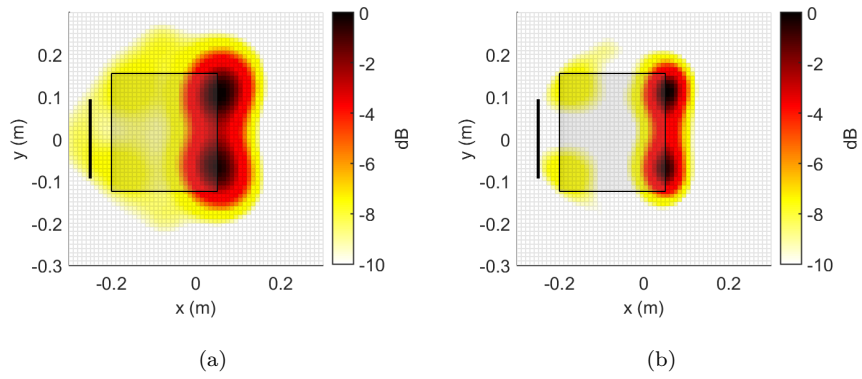

Figure 20: Acoustic maps of airfoil for 2.5 kHz one-third octave band, corresponding to $He = [8.4 - 10.5]$. (a) CB (b) OC-FB.
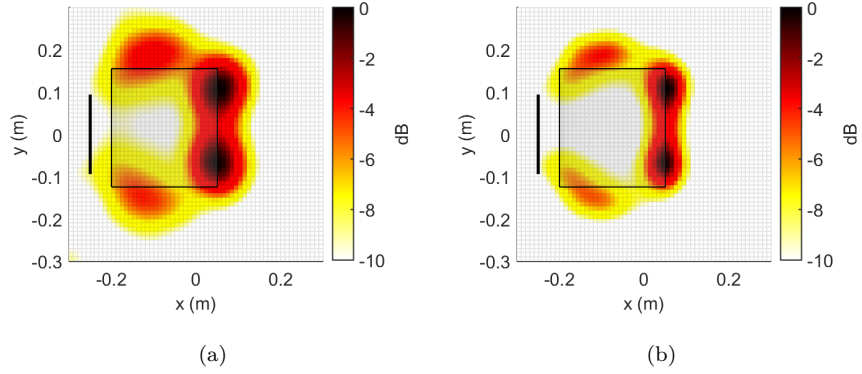
Figure 21: Acoustic maps of airfoil for 3.15 kHz one-third octave band, corresponding to $He = [10.6; 13.2]$. (a) CB (b) OC-FB.
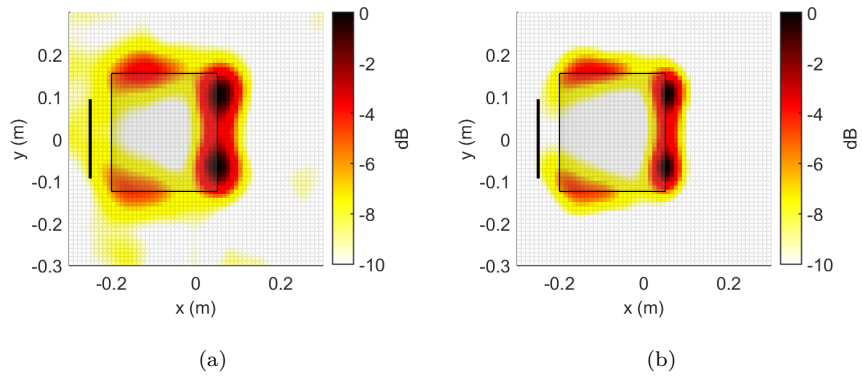

Figure 22: Acoustic maps of airfoil for 4 kHz one-third octave band, corresponding to $He = [13.4; 16.7]$. (a) CB (b) OC-FB.
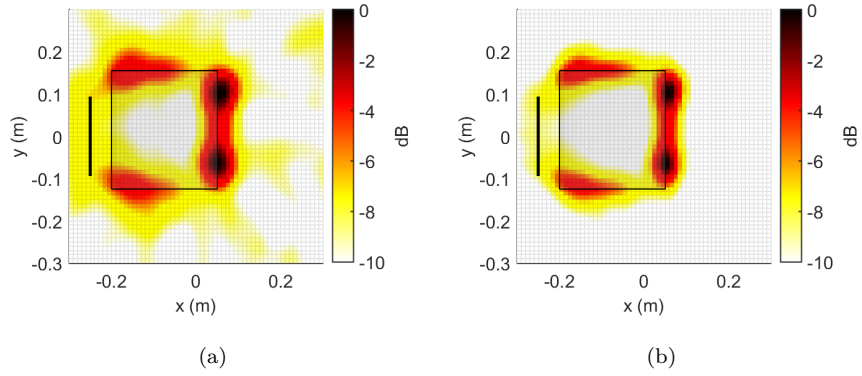
Figure 23: Acoustic maps of airfoil for 5 kHz one-third octave band, corresponding to $He = [16.8; 21.0]$. (a) CB (b) OC-FB.
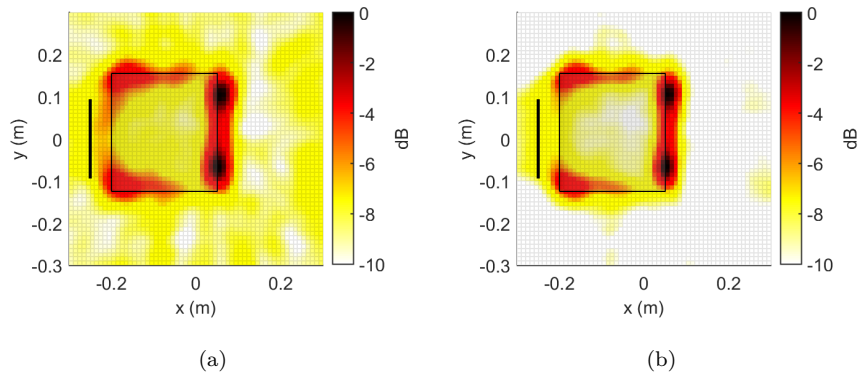

Figure 24: Acoustic maps of airfoil for 6.3 kHz one-third octave band, corresponding to the $He = [21.1; 26.4]$. (a) CB (b) OC-FB.
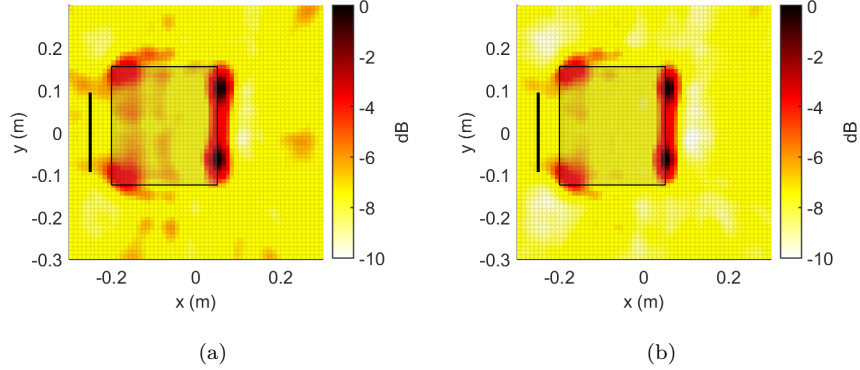
Figure 25: Acoustic maps of airfoil for 8 kHz one-third octave band, corresponding to $He =$ [26.8; 33.6]. (a) CB (b) OC-FB.

6. Conclusions

The Order Calibrated Functional Beamforming presented in this paper exploits the Functional Beamforming order as a leverage to achieve a beamformer with constant MLW over a chosen frequency range. Therefore, it is necessary to calculate the proper order ν^* as function of the frequency of analysis. With this purpose, a measurement strategy for the MLW has been discussed. This approach, compatible with FB and any mainlobe shape, makes it possible to characterise the spatial resolution of a generic planar array with respect to Helmholtz number He and beamformer order ν. The systematic characterisation of the mainlobe radius for a wide set of arrays, generated by means of the Vogel's spiral theory, revealed that its trend is weakly dependant from the array design.

Wrapping all the information gathered in this preliminary study, an Order Calibration Procedure has been proposed to obtain a relation in the form $\nu^* = f(Hn, He_{\text{ref}})$, where the definition of the normalised Helmholtz number Hn allows to generalise the approach, while the reference Helmholtz number He_{ref} can be used to set the desired beamformer resolution. The proposed pro-

33

cedure returns a simple polynomial curve that accurately represents the exact curve of the proper beamformer orders. Therefore, the characterisation of the array boils down to the estimation of two coefficients with a polynomial Least-Squares fitting. The application of OC-FB on simulated data demonstrates the effectiveness of the idea and of the OCP, while the application on aeroacoustic experimental data shows evident benefits also in challenging test cases.

One of the main achievement of the study presented here is that the calibration coefficients are weakly dependent on the choice of the reference Helmholtz number and the source position. This aspect has relevant effects on the practical exploitation of the OC-FB. In fact, once the average calibration coefficients are estimated over a variety of source positions and He_{ref}, they can be adopted in almost any usage of the given array. For this reason, OC-FB can find a place as simple strategy for performance improvement of FB with very low effort requested to the user. In fact, the order calibration can be done with little computational effort, once and for all, for a large set of application conditions. Moreover, the calibration accuracy can be scaled depending on the user needs, by changing the fitting curve or directly interpolating the calculated list of orders ν^* as a lookup table. Moreover, the idea of OC-FB is open to other possible beamformer characteristics optimisation, such as the dynamic range. Authors are working on these aspects, which will be the topics of future works.

Acknowledgements

References

₅₁₅ [1] G. Battista, G. Herold, E. Sarradj, P. Castellini, P. Chiariotti, IRLS based inverse methods tailored to volumetric acoustic source mapping, Applied Acoustics 172 (2021) 107599. `doi:10.1016/j.apacoust.2020.107599`.

[2] R. Zamponi, P. Chiariotti, G. Battista, C. Schram, P. Castellini, 3d generalized inverse beamforming in wind tunnel aeroacoustic testing: applica₅₂₀ tion to a counter rotating open rotor aircraft model, Applied Acoustics 163 (2020) 107229. `doi:10.1016/j.apacoust.2020.107229`.

[3] G. Battista, M. Vanali, P. Chiariotti, P. Castellini, A comparison between aeroacoustic source mapping techniques for the characterisation of wind turbine blade models with microphone arrays, ACTA IMEKO 10 (4) (2021) ₅₂₅ 147. `doi:10.21014/acta_imeko.v10i4.1142`.

[4] S. Jekosch, E. Sarradj, An inverse microphone array method for the estimation of a rotating source directivity, Acoustics 3 (3) (2021) 462–472. `doi:10.3390/acoustics3030030`.

[5] O. Amoiridis, R. Zamponi, A. Zarri, J. Christophe, C. Schram, Localization ₅₃₀ and characterization of rotating noise sources on axial fans by means of an irregularly shaped microphone array, Journal of Physics: Conference Series 1909 (1) (2021) 012003. `doi:10.1088/1742-6596/1909/1/012003`.

[6] P. Chiariotti, M. Martarelli, P. Castellini, Acoustic beamforming for noise source localization – reviews, methodology and applications, Mechani₅₃₅ cal Systems and Signal Processing 120 (2019) 422–448. `doi:10.1016/j.ymssp.2018.09.019`.

[7] R. Merino-Martínez, P. Sijtsma, M. Snellen, T. Ahlefeldt, J. Antoni, C. J. Bahr, D. Blacodon, D. Ernst, A. Finez, S. Funke, T. F. Geyer, S. Haxter, G. Herold, X. Huang, W. M. Humphreys, Q. Leclère, A. Malgoezar, ₅₄₀ U. Michel, T. Padois, A. Pereira, C. Picard, E. Sarradj, H. Siller, D. G. Simons, C. Spehr, A review of acoustic imaging methods using phased

microphone arrays, CEAS Aeronautical Journal 10 (1) (2019) 197–230.
`doi:10.1007/s13272-019-00383-4`.

[8] Q. Leclère, A. Pereira, C. Bailly, J. Antoni, C. Picard, A unified formalism for acoustic imaging based on microphone array measurements, International Journal of Aeroacoustics 16 (4-5) (2017) 431–456. `doi:10.1177/1475472x17718883`.

[9] P. Sijtsma, Clean based on spatial source coherence, International Journal of Aeroacoustics 6 (4) (2007) 357–374. `arXiv:https://doi.org/10.1260/147547207783359459`, `doi:10.1260/147547207783359459`.
URL `https://doi.org/10.1260/147547207783359459`

[10] T. F. Brooks, W. M. Humphreys, A deconvolution approach for the mapping of acoustic sources (DAMAS) determined from phased microphone arrays, Journal of Sound and Vibration 294 (4-5) (2006) 856–879. `doi:10.1016/j.jsv.2005.12.046`.

[11] G. Chardon, J. Picheral, F. Ollivier, Theoretical analysis of the damas algorithm and efficient implementation of the covariance matrix fitting method for large-scale problems, Journal of Sound and Vibration 508 (2021) 116208. `doi:https://doi.org/10.1016/j.jsv.2021.116208`.
URL `https://www.sciencedirect.com/science/article/pii/S0022460X21002807`

[12] J. D. Maynard, E. G. Williams, Y. Lee, Nearfield acoustic holography: I. theory of generalized holography and the development of nah, The Journal of the Acoustical Society of America 78 (4) (1985) 1395–1413. `arXiv:https://doi.org/10.1121/1.392911`, `doi:10.1121/1.392911`.
URL `https://doi.org/10.1121/1.392911`

[13] T. Suzuki, Generalized Inverse Beam-forming Algorithm Resolving Coherent/Incoherent, Distributed and Multipole Sources. `arXiv:https://arc.aiaa.org/doi/pdf/10.2514/6.2008-2954`, `doi:10.2514/6.2008-2954`.
URL `https://arc.aiaa.org/doi/abs/10.2514/6.2008-2954`

[14] T. Yardibi, J. Li, P. Stoica, L. Cattafesta, Sparsity Constrained Deconvolution Approaches for Acoustic Source Mapping. `arXiv:https://arc.aiaa.org/doi/pdf/10.2514/6.2008-2956`, `doi:10.2514/6.2008-2956`.
URL `https://arc.aiaa.org/doi/abs/10.2514/6.2008-2956`

[15] T. Yardibi, J. Li, P. Stoica, N. S. Zawodny, L. N. Cattafesta, A covariance fitting approach for correlated acoustic source mapping, The Journal of the Acoustical Society of America 127 (5) (2010) 2920–2931. `arXiv:https://doi.org/10.1121/1.3365260`, `doi:10.1121/1.3365260`.
URL `https://doi.org/10.1121/1.3365260`

[16] J. Antoni, A bayesian approach to sound source reconstruction: Optimal basis, regularization, and focusing, The Journal of the Acoustical Society of America 131 (4) (2012) 2873–2890. `arXiv:https://doi.org/10.1121/1.3685484`, `doi:10.1121/1.3685484`.
URL `https://doi.org/10.1121/1.3685484`

[17] G. Battista, P. Chiariotti, M. Martarelli, P. Castellini, Inverse methods in aeroacoustic three-dimensional volumetric noise source localization and quantification, Journal of Sound and Vibration 473 (2020) 115208. `doi:10.1016/j.jsv.2020.115208`.

[18] G. Battista, P. Chiariotti, M. Martarelli, P. Castellini, C. Colangeli, K. Janssens, 3d acoustic mapping in automotive wind tunnel: Algorithm and problem analysis on simulated data, Applied Sciences 11 (7) (2021) 3241. `doi:10.3390/app11073241`.

[19] B. V. Veen, K. Buckley, Beamforming: a versatile approach to spatial filtering, IEEE ASSP Magazine 5 (2) (1988) 4–24. `doi:10.1109/53.665`.

[20] Dougherty, Functional beamforming, in: Proceedings on CD of the 5th Berlin Beamforming Conference, 19-20 February 2014, GFaI, Gesellschaft zu Förderung angewandter Informatik e.V., Berlin, 2014.
URL `http://bebec.eu/Downloads/BeBeC2014/Papers/BeBeC-2014-01.pdf`

[21] P. Welch, The use of fast fourier transform for the estimation of power spectra: A method based on time averaging over short, modified periodograms, IEEE Transactions on Audio and Electroacoustics 15 (2) (1967) 70–73. `doi:10.1109/TAU.1967.1161901`.

[22] P. Chiariotti, G. Battista, M. Ettorre, P. Castellini, Average acoustic beamforming in car cabins: An automatic system for acoustic mapping over 3d surfaces, Applied Acoustics 129 (2018) 47–63. `doi:10.1016/j.apacoust.2017.07.009`.

[23] E. Sarradj, Three-dimensional acoustic source mapping with different beamforming steering vector formulations, Advances in Acoustics and Vibration 2012 (2012) 1–12. `doi:10.1155/2012/292695`.

[24] L. T. L. Pereira, R. Merino-Martínez, D. Ragni, D. Gómez-Ariza, M. Snellen, Combining asynchronous microphone array measurements for enhanced acoustic imaging and volumetric source mapping, Applied Acoustics 182 (2021) 108247. `doi:10.1016/j.apacoust.2021.108247`.

[25] Sarradj, A Generic approach to syntthesize optimal array microphone arrangements, in: Proceedings on CD of the 6th Berlin Beamforming Conference, 29 February - 1 March 2016, GFaI, Gesellschaft zu Förderung angewandter Informatik e.V., Berlin, 2016.
URL `http://www.bebec.eu/Downloads/BeBeC2016/Papers/BeBeC-2016-S4.pdf`

[26] Baron, Finez, Nicolas, Numerical and experimental assessment of functional beamforming for source quantification, in: Proceedings on CD of the 7th Berlin Beamforming Conference, March 5-6, 2018, GFaI, Gesellschaft zu Förderung angewandter Informatik e.V., Berlin, 2018.
URL `http://www.bebec.eu/Downloads/BeBeC2018/Papers/BeBeC-2018-S08.pdf`

[27] R. Merino-Martínez, M. Snellen, D. G. Simons, Functional beamforming

applied to imaging of flyover noise on landing aircraft, Journal of Aircraft 53 (6) (2016) 1830–1843. `doi:10.2514/1.c033691`.

[28] J. Hald, Removal of incoherent noise from an averaged cross-spectral matrix, The Journal of the Acoustical Society of America 142 (2) (2017) 846–854. `doi:10.1121/1.4997923`.

[29] A. Dinsenmeyer, J. Antoni, Q. Leclère, A. Pereira, A probabilistic approach for cross-spectral matrix denoising: Benchmarking with some recent methods, The Journal of the Acoustical Society of America 147 (5) (2020) 3108–3123. `arXiv:https://doi.org/10.1121/10.0001098`, `doi:10.1121/10.0001098`.
URL `https://doi.org/10.1121/10.0001098`

[30] G. Battista, P. Chiariotti, P. Castellini, Spherical harmonics decomposition in inverse acoustic methods involving spherical arrays, Journal of Sound and Vibration 433 (2018) 425–460. `doi:10.1016/j.jsv.2018.05.001`.

[31] D. Johnson, D. Dudgeon, Array Signal Processing: Concepts and Techniques, Prentice-Hall Series in Signal, P T R Prentice Hall, 1993.
URL `https://books.google.nl/books?id=v_NSAAAAMAAJ`

[32] G. Herold, T. F. Geyer, E. Sarradj, Comparison of Inverse Deconvolution Algorithms for High-resolution Aeroacoustic Source Characterization. `arXiv:https://arc.aiaa.org/doi/pdf/10.2514/6.2017-4177`, `doi:10.2514/6.2017-4177`.
URL `https://arc.aiaa.org/doi/abs/10.2514/6.2017-4177`

[33] G. Herold, E. Sarradj, Open-source software for the application of microphone array methods, Noise & Vibration Worldwide 48 (3-4) (2017) 44–51. `arXiv:https://doi.org/10.1177/0957456517699024`, `doi:10.1177/0957456517699024`.
URL `https://doi.org/10.1177/0957456517699024`